Open-boundary reflection of quantum well states at Pb(111)

M. Müller,[1] N. Néel,[1] S. Crampin,[2,*] and J. Kröger[1,†]

[1]*Institut für Physik, Technische Universität Ilmenau, D-98693 Ilmenau, Germany*
[2]*Department of Physics & Centre for Nanoscience and Nanotechnology, University of Bath, Bath BA2 7AY, UK*

Using a scanning tunneling microscope, confined electron states are studied that exist above subsurface nanometer-sized voids at Pb(111), where potential barriers at the parallel vacuum–Pb(111) and Pb(111)–void interfaces establish a principal series of quantum well states that are further confined laterally by strong reflection at the open boundaries at the edges of the void. The influence of the size, depth and shape of the voids on the effectiveness of the lateral confinement is discussed. Standing wave patterns observed in differential conductance maps unravel the dispersion of the relevant underlying Pb electron states.

I. INTRODUCTION

Restricting the motion of electrons in metals or semiconductors to dimensions that are comparable to the Fermi wavelength λ_F is referred to as quantum confinement. The resulting quantization of electron states can alter the physical properties of the solid, in ways beneficial to a variety of applications including spintronics,[1] quantum computing,[2] optoelectronics,[3,4] photovoltaics,[5] and catalysis.[6] An important example of quantum confinement is within quantum wells formed in thin films and overlayers. While electrons in these systems are able to move freely in the plane of the film, the film–substrate and/or film–vacuum interfaces act as barriers, reflecting impinging electrons. At specific film thicknesses standing electron waves are established between the interfaces, giving rise to quantum well states (QWS). Since the first experimental evidence for QWS was reported, using the reflection of low-energy electrons from Au films deposited on Ir(111),[7] there has followed a wealth of experimental and theoretical work on QWS for a wide variety of film–substrate combinations,[8] and the importance of QWS has been unraveled for, amongst others, monitoring film quality,[9] chemical reactivity,[10,11] crystal growth,[12] magnetic interactions,[13–15] and electron correlation effects such as thin-film superconductivity[16–18] and the Kondo effect.[19,20]

Lateral electron confinement to two dimensions has likewise been observed, with real-space images of surface electron standing waves in the vicinity of noble-metal step edges[21–23] constituting seminal work that has seen artificially fabricated atom assemblies used as quantum corrals for electronic surface states,[24–26] and nanometer-scaled clusters,[27,28] vacancies[29,30] and molecular networks[31,32] shown to effectively confine electron motion. Laterally confined surface states have also been observed on narrow terraces[33] and vicinal surfaces,[34–36] and recently electron confinement to graphene nanostructures has attracted considerable interest.[37–42]

Further restriction of electron motion has been reported for atomic[43–48] and molecular[49,50] chains on surfaces, defects on semiconductor surfaces,[51] colloidal semiconductor nanocrystals,[52] metal[53] and semiconductor[54] quantum dots as well as for artificial atoms.[55] A beautiful demonstration of electron confinement is the observation of the quantum analogue to whispering gallery modes in oligothiphene rings[56] and graphene.[57]

The aforementioned examples reveal the panoply of confinement effects, and highlight an important shared ingredient: for electron motion to be restricted to a specific region of space requires an effective potential well, enclosed by boundaries that reflect electron waves. The confining potential wells may be provided by geometric constraints, such as boundaries of terraces and quantum corrals, atomic and molecular chain edges, and by the forbidden electron penetration into the vacuum or surface-projected energy gaps of the substrate.

We have recently reported a novel confinement mechanism affecting the conduction electrons of a metal,[58] observed in the vicinity of nanometer-sized subsurface voids (or "cavities") at Pb(111). These cavities were engineered by Ar^+ ion bombardment and subsequent annealing, and are located several atomic layers beneath the Pb(111) surface. Similar structures have previously been reported for Al(111),[59] Cu(100),[60–62] Cu(110),[61,63] Ag(100)[64] and Ag(111)[64] surfaces. The voids offer a unique opportunity to investigate vertical and lateral confinement, with vertical confinement occuring in the thin Pb layer atop the void where the parallel void–Pb(111) and Pb(111)–vacuum interfaces lead to the formation of conventional QWS, and additionally reflection of electrons at the open boundaries where the thin Pb film above the void recovers its bulk thickness resulting in lateral confinement. The latter is noteworthy in occuring despite the absence of a confining potential well in the lateral direction. The purpose of the present article is to expand upon our previous reported findings. Real-space images of electron standing wave patterns associated with the confinement are provided and used to extract the relevant Pb band dispersion. In addition, a study of the influence of the cavity size and distance beneath the substrate surface on the confined states is presented.

II. EXPERIMENT

Experiments were performed with a scanning tunneling microscope (STM) operated in ultrahigh vacuum (10^{-9} Pa) and at low temperature (6 K). Atomically clean Pb(111) was obtained by repeated Ar^+ bombardment and annealing. To efficiently create subsurface voids the ion kinetic energy and current density at the sample were set to 1.1 keV and $5\,\mu A/cm^2$, respectively, with the ion beam impinging onto the surface at an angle of 30° with respect to the surface normal. Samples were subsequently annealed at 560 K for 20 min. All STM

images were recorded at constant current with the bias voltage applied to the sample. Spectra of the differential conductance (dI/dV) were acquired at constant height by sinusoidally modulating the sample voltage ($5\,mV_{pp}$, $6.3\,kHz$) and detecting the current response of the junction with a lock-in amplifier. For recording maps of dI/dV simultaneously with STM images a higher voltage modulation ($20\,mV_{pp}$) was used.

III. MODELING

The electronic structure of thin Pb(111) films has been calculated using density functional theory, using the plane wave pseudopotential code CASTEP.[65] *Ab-initio* energy bands for film thickness between 2 and 14 layers have been calculated using both the local-density approximation and the general-gradient approximation to the exchange functional, default "on-the-fly" ultrasoft pseudopotentials, 240 eV plane wave basis cutoff energy, $41\times41\times1$ Monkhorst-Pack k-point grids and a 15 Å vacuum gap. Geometry optimization minimized forces to $<0.05\,eV/Å$.

In Ref. 58 confinement *via* open-boundary scattering was modeled using an idealized model, treating Pb as a free-electron metal and with voids described as cylindrically symmetric volumes from which electrons were fully excluded, with radius S and extending from a depth D beneath the surface. The Pb(111) surface barrier was similary modeled by an infinite step-potential. Here we supplement that model, which permits analytic analysis, with numerical results obtained for a more general description in which the void and surface barrier are described by finite potential barriers and with more varied void geometries. In the region outside both the surface barrier (assumed planar and occupying $z<0$) and the nanovoid we assume free-electron propagation. We determine the electronic structure from the single-particle Green function $G(\boldsymbol{r},\boldsymbol{r}';\varepsilon)$ satisfying $(\mathcal{H}-\varepsilon)G=-\delta(\boldsymbol{r}-\boldsymbol{r}')$, which for $z<z'$ has the form (energy dependence suppressed)

$$G(\boldsymbol{r},\boldsymbol{r}')=\sum_{MM'}\int dk\int dk'\Psi^{<}_{Mk}(\boldsymbol{r})\,\mathcal{G}_{MM'}(k,k')\Psi^{>}_{M'k'}(\boldsymbol{r}')/(i\kappa') \tag{1}$$

where in the region of constant potential between the surface barrier and void potential, the wave functions $\Psi^{>}$ and $\Psi^{<}$ are

$$\begin{aligned}\Psi^{<}_{Mk}(\boldsymbol{r})&=\chi^{-}_{Mk}(\boldsymbol{r})+\chi^{+}_{Mk}(\boldsymbol{r})\,\mathcal{L}(k)\\ \Psi^{>}_{Mk}(\boldsymbol{r})&=\chi^{+\times}_{Mk}(\boldsymbol{r})+\sum_{M'}\int dk'\,\mathcal{R}_{MM'}(k,k')\chi^{-\times}_{M'k'}(\boldsymbol{r}),\end{aligned} \tag{2}$$

corresponding to combinations of forward (+) and backward (−) travelling cylindrical waves,

$$\chi^{\pm}_{Mk}(\boldsymbol{r})=\chi_{Mk}(\boldsymbol{R})e^{\pm i\kappa z},\quad \chi_{Mk}(\boldsymbol{R})=\sqrt{k/2\pi}J_M(kR)e^{iM\varphi} \tag{3}$$

where $\boldsymbol{r}=(R,\varphi,z)$, $\boldsymbol{R}=(R,\varphi)$, k the wave number in the plane perpendicular to $\hat{\boldsymbol{z}}$, J_M a cylindrical Bessel function, angular momentum quantum number $M\in\mathbb{Z}$, $\kappa=\sqrt{2\varepsilon-k^2}$, and in Eq. (2) $\times$ denotes conjugation of the angular factor only. The void is assumed to be centered laterally at $R=0$. $\mathcal{L}$ and $\mathcal{R}$ are barrier and void reflection coefficients, respectively, with $\mathcal{L}$ in general found by numerical integration of the one-dimensional Schrödinger equation: for a step barrier, height w at $z=0$, $\mathcal{L}=(i\kappa-\gamma)/(i\kappa+\gamma)$ with $\gamma=\sqrt{2(w-\varepsilon)+k^2}$. The void reflection coefficient $\mathcal{R}$ is calculated using the method outlined in the appendix. In Eq. (1) $\mathcal{G}$ is obtained from the integral equation expressed formally as $\mathcal{G}=1+\mathcal{R}\mathcal{L}\,\mathcal{G}$.

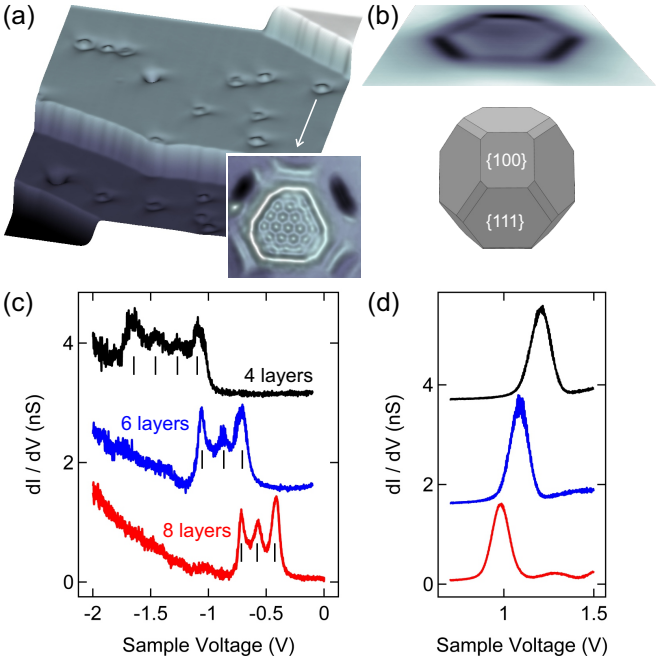

FIG. 1. (Color online) (a) Pseudo three-dimensional STM image of Pb(111) revealing cavities buried beneath two terraces (0.5 nA, 1.2 V, 1000 Å × 1000 Å). Inset: Constant-current map of dI/dV recorded atop the indicated cavity showing electron standing wave patterns (1 nA, 0.4 V, 78 Å × 78 Å). (b) Schematic illustration of a subsurface nanocavity, with geometry based upon the Wulff construction using (111), (110) and (100) Pb surface energies. {111} and {100} facets are indicated; {110} facets appear as the smallest regions of the Wulff construction. (c) Spectra of dI/dV acquired atop the center of cavities with similar radii of ≈ 20 Å residing at the indicated depths, and showing the signature of the HOQWS. The spectra for 6 and 4 layers have been vertically offset by 1.5 nS and 3 nS, respectively. The vertical bars indicate the spectroscopic fine structure due to lateral confinement. Prior to data acquisition the feedback loop had been disabled at 1 nA, −2 V for all spectra. (d) As (c), showing the spectroscopic signatures of the LUQWS. The spectra for 6 and 4 layers have been vertically offset by 1.6 nS and 3.7 nS, respectively. The feedback loop had been disabled at 0.5 nA, 2.3 V prior to data acquisition.

IV. RESULTS AND DISCUSSION

A. Geometric and electronic properties of buried cavities

Figure 1(a) shows the pseudo-three-dimensional STM image of a freshly prepared Pb(111) surface. Buried cavities reveal themselves as depressions or protrusions with an irregular

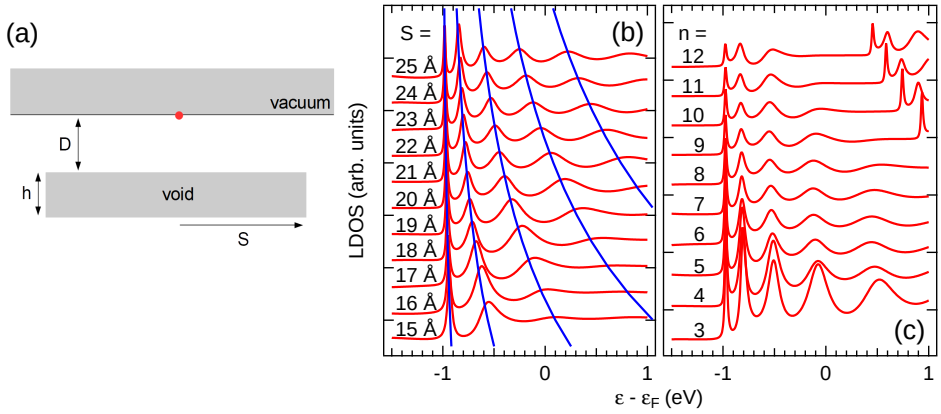

FIG. 2. (Color online) Lateral confinement. (a) Model geometry. A cylindrically symmetric void of radius S, thickness h is positioned a depth D beneath the surface. Gray regions correspond to potential v. The red dot indicates the position at which the LDOS is evaluated. (b) Calculated LDOS atop voids (height $h = 8\,\text{Å}$, depth $D = 11.4\,\text{Å}$, potential $v = 13.6\,\text{eV}$). Results obtained for different radii S are offset vertically (red). Also shown (blue) are the expected peak positions assuming ideal reflection at the void edge (see text). (c) Calculated LDOS above voids (cylindrical volume, $h = 8\,\text{Å}$, $S = 23\,\text{Å}$, $v = 13.6\,\text{eV}$) at various depths. Each spectrum (vertically offset) is calculated with the void at a depth placing the onset of the nth lowest QWS at energy $\varepsilon_n = \varepsilon_\text{F} - 1.0\,\text{eV}$.

hexagonal circumference, and apparent diameters that range between 25 and 70 Å. Their geometric structure reflects the minimized interfacial free energy according to the Wulff construction [Fig. 1(b)]. The upper $\{100\}$ and $\{111\}$ side facets of the cavity scatter electrons and give rise to interference effects, with the characteristic fringes visible both in Fig. 1(b) and outside the central confinement pattern present in the inset to Fig. 1(a) similar to those previously observed and reported for subsurface cavities at Cu(110).[63]

The parallel Pb(111) surface and upper face of the void form an electron resonator that quantizes the electron states according to their variation in the direction normal to the surface. The energies of these QWS depend strongly on the Pb layer thickness, so that the location and spacing of the highest occupied QWS (HOQWS) [Fig. 1(c)] and lowest unoccupied QWS (LUQWS) [Fig. 1(d)] of these states provide a signature of the depth of the void. This depth is identified by comparison with calculated *ab-initio* thin-film energy bands. The most abundant Pb film thicknesses deduced above the buried voids are 4, 6 and 8 atomic layers, indicating a preference for even numbers of Pb atomic layers and an electronic stabilization effect influencing the void depth. Indeed, the Fermi wavelength λ_F of Pb electron states propagating perpendicular to the (111) surface is approximately four times the (111) layer–layer spacing and therefore a bilayer periodicity of the density of states at the Fermi energy, ε_F, may be expected. Bilayer periodicity in other Pb thin-film properties have likewise been reported, including the superconducting transition temperature in ultrathin Pb films,[16–18] preferred island heights[66,67] and the work function.[68]

The $\text{d}I/\text{d}V$ spectra acquired atop the center of nearly equally sized ($S \approx 20\,\text{Å}$) cavities at different depths [Fig. 1(c)] show that the bias voltage range of the feature associated to the HOQWS decreases from $\approx 0.7\,\text{V}$ (4 layers) *via* $\approx 0.45\,\text{V}$ (6 layers) to $\approx 0.35\,\text{V}$ (8 layers) as the feature moves to zero bias voltage with increasing Pb film thickness. The broad but finite line shape of the HOQWS is due to hybridization between Bragg-diffracted states that cause the band structure of thin Pb films to exhibit an increasing effective mass for increasing QWS energy.[69,70] Concomitantly the band width decreases with increasing QWS energy, as seen in Fig. 1(c) and in the broader appearance of the HOQWS than the LUQWS [Fig. 1(d)] for a given film thickness.[71] Characteristic spectroscopic fine structure is clearly visible within the band width of the HOQWS, indicated by vertical bars in Fig. 1(c). These arise from lateral confinement of the QWS electrons to the region atop the cavity,[58] and are discussed in the following section. It is noteworthy that spectra such as those in Fig. 1(c) recorded at temperatures above and below the critical temperature of Pb (7.2 K) show no significant differences, confirming that the superconducting state of Pb is not relevant to these findings.

The inset to Fig. 1(a) displays a constant-current $\text{d}I/\text{d}V$ map recorded above the indicated cavity, revealing rich structure with a regular hexagonal pattern visible in the central area. The size ($\gtrsim 7\,\text{Å}$) and voltage dependence of the pattern points to an electronic origin, which we attribute to the quantum interference pattern resulting also from reflection of QWS electrons at the open boundary where the thin Pb film between the cavity and the Pb(111) surface recovers its bulk thickness. Analysis of these patterns is used to extract the dispersion of the underlying electron bands — *vide infra*.

B. Lateral confinement

In Ref. 58 the fine structure present in $\text{d}I/\text{d}V$ spectra recorded atop subsurface voids was recognized as resulting from further lateral confinement of the principally vertically-confined QWS electrons, due to open-boundary reflection at

the edges of the void. Here, the nature of this confinement is further explored. We report results obtained using steplike potentials for both surface barrier (at $z = 0$) and void, the latter presenting a face a distance D from the surface [Fig. 2(a)]. The local density of states (LDOS) is obtained from the Green function calculated as described in Sec. III as $n(\boldsymbol{r};\varepsilon) = -(1/\pi)\mathrm{Im}G(\boldsymbol{r},\boldsymbol{r};\varepsilon)$.

Figure 2(b) shows $n(\boldsymbol{r} = 0,\varepsilon)$ atop cylindrically shaped voids of varying radii S, fixed thickness $h = 8$ Å, located at a constant depth $D = 11.4$ Å. Increasing the thickness has no effect on the results. A void potential of strength $v = 13.6$ eV and $\varepsilon_F = 9.47$ eV for Pb is used giving rise to the HOQWS, the 6th lowest QWS at this depth, at threshold energy $E_6 = \varepsilon_F - 1.0$ eV. For $S = \infty$, corresponding to an infinitely extended thin film, the LDOS associated with the QWS takes on the appearance of a steplike increase at energy E_6 (not shown), broadened slightly by the 5 meV imaginary energy included in calculations for numerical purposes. Unlike the experimental spectra of Fig. 1(c) there is no upper band edge, as the model does not contain Bragg-diffraction effects, only free-electron like dispersion. As evident in Fig. 2(b), atop voids of finite radius the LDOS within the QWS subband instead takes on the appearance of a series of resonant peaks, with the jth peak occuring at

$$\varepsilon_j = E_6 + \frac{\hbar^2}{2m}\left(\frac{\alpha_{j,0}}{S}\right)^2, \qquad (4)$$

where $\alpha_{j,0}$ ($= 2.405, 5.520, 8.654, \ldots$ for $j = 1,2,3,\ldots$) is the jth zero of the Bessel function J_0. The blue curves in Fig. 2(b) trace out the relationship of Eq. (4). The origin of this behavior lies in strong reflection of laterally-outward travelling free-electron like states present in the region above the void, at the radius S where the opening up of the full depth of the Pb crystal acts like a hard-wall boundary. This has the effect of imposing a node in the radial wave function $J_M(kR)$ at $R = S$, quantizing the wave number k. Only states with $M = 0$ additionally have nonvanishing amplitude at $R = 0$, and so contribute to the LDOS at $\boldsymbol{r} = 0$, and hence the existence of quantized energies given by Eq. (4). The levels are resonances due to the lossy-character of the boundary reflection, with the variation in the peak widths due to the combined effects of the energy dependence of the losses and the increasing boundary collision rate with energy.[58]

Next, the effect of the depth of the void is unveiled. To do this, we exploit the continuum nature of our model to position voids at a succession of depths D_n that each place the nth QWS at the same threshold energy $\varepsilon_F - 1.0$ eV (*e. g.*, $D_n = 9.3$ Å, 11.4 Å, 13.5 Å for $n = 5$, 6, 7). The corresponding spectra are shown in Fig. 2(c). The radius and thickness of the cylindrical void are held fixed, with $S = 23$ Å and $h = 8$ Å, respectively. The energy spacing of the principal series of QWS associated with confinement normal to the surface decreases with increasing void depth, such that the spectra calculated for depth D_9 and above also show the LUQWS in the energy range displayed.

It can be seen from Fig. 2(c) that the location of spectral features within the QWS subband are not sensitive to the depth of the void. This is consistent with their origin being energy quantization associated with electron confinement caused by open-boundary reflection at the edge radius, which is unchanging. However, the width of the resonances that make up the spectra do change, becoming broader with increasing void depth, such that whereas the first 5 peaks are clearly resolvable for the depth D_3, this drops to only 3 for D_{12} ($= 24.1$ Å). Therefore, the effects of lateral confinement are visible above voids whose depth is comparable to the void radius, but the effectiveness of the confinement decreases with void depth, due to an increase in the lossy character of the elastic boundary scattering.[30,72,73] One consequence of this is that the use of subsurface voids to induce spectral structure from which intrinsic electron-electron and electron-phonon scattering rates can be deduced[58] will be limited to shallower voids, else elastic scattering effects will dominate linewidths and prevent the smaller intrinsic lifetime effects from being extracted.

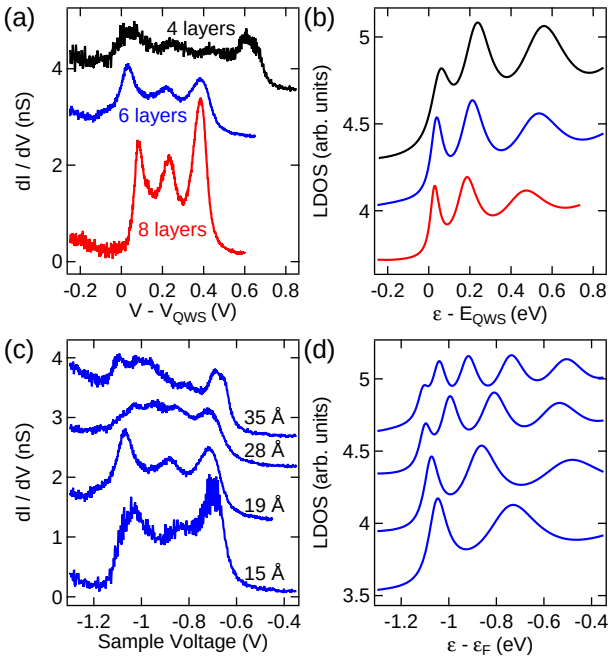

FIG. 3. (Color online) Voids of similar size at different depths, and with different radii at the same depth. (a) dI/dV spectra acquired atop the center of voids with radii ≈ 20 Å and indicated depths. The bias voltage (V) of each spectrum was adjusted in order to align the onset of the QWS ($V_{QWS} = 1.7$ V, 1.1 V, 0.8 V for 4, 6, 8 layers, respectively). The dI/dV data for 4 (6) layers were vertically offset by 3.4 nS (2.5 nS). The feedback loop was disabled at 1 nA, -2 V (4 layers), -1.75 V (6 layers), -1.2 V (8 layers). (b) Calculated LDOS for cylindrical cavity ($h = 8$ Å, $S = 21$ Å) 4 (top), 6 (middle), 8 (bottom) layers beneath the Pb(111) surface. The energy axis was adjusted to align the QWS onsets. The top and middle spectra were vertically offset for clarity. (c) dI/dV spectra acquired atop the center of voids buried 6 layers beneath the Pb(111) surface and with indicated radii. The spectra were vetically offset by 1.2 nS (19 Å), 2 nS (28 Å), 2.6 nS (35 Å). Feedback loop parameters: 1 nA, -1.5 V (15 Å, 28 Å, 35 Å), -1.75 V (19 Å). (d) Calculated LDOS for cylindrical cavity ($h = 8$ Å) with radii (from bottom to top) 15 Å, 19 Å, 28 Å, 35 Å and 6 layers beneath the Pb(111) surface. Data were vertically offset for clarity.

The calculations nicely reproduce spectroscopic data obtained from buried voids. Figures 3(a), (b) compare experimental [Fig. 3(a)] and calculated [Fig. 3(b)] data for voids with similar radii $S = 20 \pm 2$ Å and buried 4, 6, 8 layers beneath the Pb(111) surface. All spectra show the HOQWS whose covered bias voltage and calculated energy ranges have been shifted by the QWS onset voltage and energy to facilitate the comparison. The additional feature in the experimental 4-layer dI/dV spectrum slightly below 0.5 V [Fig. **??**(a), top] is absent from the calculated LDOS. As previously shown,[58] such additional low-amplitude peaks are consistent with expected contributions from lower-symmetry states at slightly off-center locations above voids in the spectroscopy experiments. A similarly good agreement between experiment and theory is achieved for 4-layer deep voids with different radii [Fig. 3(c), (d)].

The actual voids in face-centered cubic (fcc) Pb have a polyhedral shape, with sloping edges, whereas the cylindrical model discussed hitherto presents an abrupt transition in Pb thickness at radius S. To understand the effect of a more gradual transition, we have also calculated the LDOS atop cylindrically symmetric voids whose radius increases from 15 Å on the upper face to 23 Å, with the angle of side slope varying between $\theta = 0°$ and 45° [Fig. 4(a)]. $\theta = 0$ is equivalent to a cylinder of radius 23 Å, whilst for $\theta = 45°$ the full width of 23 Å is reached at a depth 8 Å beneath the upper face. Figure 4(b) shows the resulting LDOS at $\boldsymbol{r} = 0$ above the center of the void. For the very shallowest of slopes ($\theta \lesssim 1°$) the spectrum consists of 5 resonant levels, similar to that associated with an ideal cylinder of radius $S = 23$ Å, but it then evolves rapidly over a narrow range of slopes (angles $1° \lesssim \theta \lesssim 7°$), after which for slopes with $\theta \approx 14°$ and above the spectrum consists of 3 peaks and has the appearance of that found above an ideal cylinder with radius $S = 15$ Å, there being very little difference in the position and width of the lowest resonances. These results indicate that sloping edges inclined at angles above $\theta \approx 14°$ reflect electrons similarly to abrupt edges, especially within ~ 0.5 eV of the band edge. The polyhedral voids within the fcc Pb crystal, Fig. 1(b), have facets that slope at angles of 54.7° ({111}, {100}) and 35.3° ({110}), and so fall within this category. Lateral confinement is to the area above the upper hexagonal face of the polyhedral void.

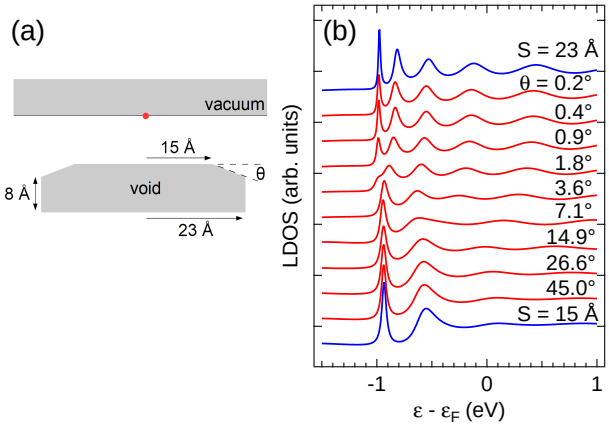

FIG. 4. (Color online) Effect of void profile. (a) Model geometry. The radius of the cylindrically-symmetric void increases from 15 Å to 23 Å at a slope angle θ, with base thickness of 8 Å. Shaded regions correspond to potential v. The red circle indicates the position at which the LDOS is evaluated. (b) Calculated LDOS atop the center of cylindrical voids with sloping edges, at depth $D = 11.4$ Å. Spectra calculated with different slope angles θ (red) are offset for clarity. Also shown for reference are the calculated spectra atop voids of uniform radii $S = 15$ Å and $S = 23$ Å (blue), at depth $D = 11.4$ Å.

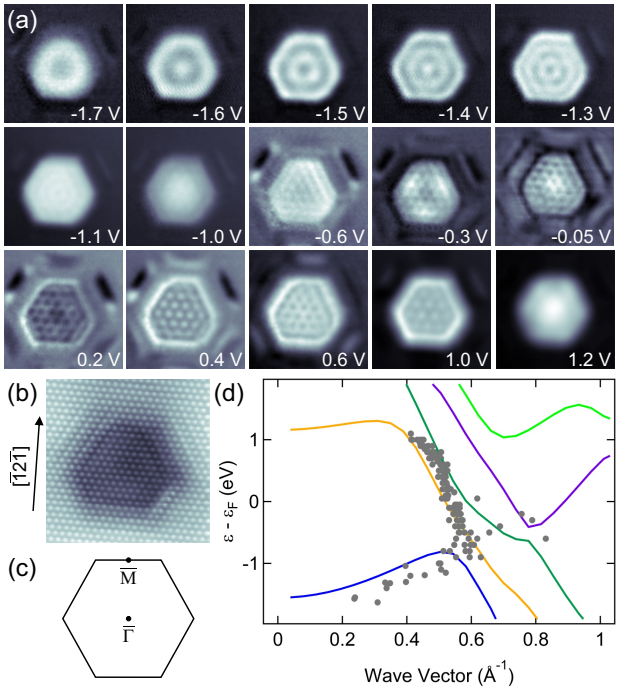

FIG. 5. (Color online) Dispersion of QWS. (a) Gallery of constant-current dI/dV maps recorded atop a cavity buried 4 atomic layers beneath the Pb(111) surface at the indicated voltages (1 nA, 78 Å × 78 Å). (b) Atomically resolved STM image of the surface region atop a buried cavity with indicated direction (0.5 nA, 0.3 V, 78 Å × 78 Å). (c) Surface Brillouin zone of Pb(111) with indicated high-symmetry points. (d) Experimental (dots) and calculated (lines) QWS band dispersion. Experimentally, the wave vector was extracted from the relevant periodicities visible in the dI/dV maps of six different cavities. The calculations were performed for a 4-layer Pb(111) thin film. The wave vector is oriented along the $\bar{\Gamma}\bar{\mathrm{M}}$ direction of the surface Brillouin zone, corresponding to the $\langle \bar{1}2\bar{1} \rangle$ crystallographic direction of Pb(111).

C. Quantum well state dispersion

Figure 5(a) presents a collection of voltage-dependent constant-current dI/dV maps measured above a 4-layer deep void. The voltage range spans the HOQWS [onset ≈ -1.7 V, Fig. 1(c)] and the LUQWS [onset ≈ 1.1 V, Fig. 1(d)]. From -1.7 V to -1.1 V the central interference pattern resembles a set of concentric rings, whose number increases with increasing voltage. Around -1.0 V the pattern is rather feature-

less. For bias voltages $\geq -0.6\,\mathrm{V}$ the standing wave pattern suddenly takes on a more complex appearance, presenting a hexagonal arrangement of antinodes whose pitch *decreases* with increasing voltage. These observations are indicative of two different electron bands — one dispersing upward, the other downward — being involved in the standing wave patterns.

In order to corroborate this idea the mutual distances between nodes and antinodes of electron standing wave patterns such as those presented in Fig. 5(a) were determined along $\langle\bar{1}2\bar{1}\rangle$ [Fig. 5(b)], which corresponds to the $\overline{\Gamma}\overline{\mathrm{M}}$ direction in reciprocal space [Fig. 5(c)]. These distances were identified with $\lambda/2$, where λ is the electron wavelength. Figure 5(d) shows the resulting experimentally extracted dispersion (dots) where $\varepsilon - \varepsilon_\mathrm{F} = eV$ (e: elementary charge) is plotted versus the wave vector $2\pi/\lambda$. The full lines in Fig. 5(d) present the calculated band structure of a 4-layer thick Pb(111) thin film along $\overline{\Gamma}\overline{\mathrm{M}}$. The HOQWS (LUQWS) dispersion is shown by a blue (orange) line. The HOQWS exhibits a nearly free-electron dispersion for small wave vectors ($< 0.5\,\mathrm{\AA}^{-1}$) but beyond this it first flattens, and then disperses downwards, with an upper band edge at around $-0.8\,\mathrm{eV}$. Above this, the states within the Pb thin film are derived from downward dispersing Bragg-diffracted bands. This explains the crossover in behavior exhibited in the $\mathrm{d}I/\mathrm{d}V$ maps Fig. 5(a). Below $\approx -0.8\,\mathrm{eV}$ the maps are associated with free-electron like states whose behavior is similar to that descibed by our earlier model. They are confined by reflection at the hexagonal edges of the upper face of the polyhedral voids, which act as a hard-wall potential. Hence the close similarity in the appearance of the maps with those observed above hexagonal islands on Ag(111),[27] which also have an interpretation in terms of confined free-electron like states, in that case Shockley surface states confined by the rapid rise in the potential at the geometrical edges of the islands.

Maps of $\mathrm{d}I/\mathrm{d}V$ around $\approx -1\,\mathrm{V}$ [Fig. 5(a)] do not show clearly resolved interference patterns, due to the rather flat energy band at that energy, meaning electron states with various wave vectors and similar energies will contribute to the interference pattern, resulting in a smeared $\mathrm{d}I/\mathrm{d}V$ map. Above $-0.6\,\mathrm{V}$ the responsible electronic states suddenly derive from a different energy band, hence the sudden change in complexity, of the $\mathrm{d}I/\mathrm{d}V$ maps, and the rather steep downward dispersion of the band accounts for the decreasing pitch of the antinodes for increasing voltage. The states associated with this band have very different character to the free-electron like states of the HOQWS, but evidently also experience reflection at the open boundary at the void edge, manifested by the resulting interference pattern. Finally, at $1.2\,\mathrm{V}$ the pattern becomes smeared out again as the voltage coincides with the flat portion of the LUQWS band.

V. SUMMARY

To summarize, we have presented results from a study of the confined electron states present above subsurface nanometer-sized voids at Pb(111), formed by Ar^+ bombardment and annealing. In the Pb above the void, the parallel vacuum–Pb(111) and Pb(111)–void interfaces form a resonator system establishing a principal series of QWS that we study using an STM. Electrons in the QWS are also confined laterally by strong reflection at the open boundaries at the edges of the void, giving rise to fine structure in $\mathrm{d}I/\mathrm{d}V$ spectra. Modeling shows that the lateral confinement is most effective for larger, shallower voids, and that the sloping edges of the polyhedral voids act as abrupt edges. $\mathrm{d}I/\mathrm{d}V$ maps recorded above buried voids reveal detailed interference patterns, with a sudden change in complexity understood in terms of the dispersion of the underlying Pb thin film states.

ACKNOWLEDGMENTS

Financial support by the Carl Zeiss Foundation and the Deutsche Forschungsgemeinschaft through KR 2912/10-1 is acknowledged. This research made use of the Balena High Performance Computing (HPC) Service at the University of Bath.

Appendix: Void reflectivity

We calculate the reflectivity $\mathcal{R}$ of the void potential by dividing it into n slices of thickness d, and determining the total reflectivity from the scattering properties of the individual slices. Slice j corresponds to the region with $|z - z_j| < d/2$, and in isolation scatters incident forward $(+)$ or backward $(-)$ travelling cylindrical waves as

$$\Psi^+_{Mk}(\boldsymbol{r}) = \begin{cases} \chi^+_{Mk}(\boldsymbol{r}_j) + \sum_{M'} \int dk' \chi^-_{M'k'}(\boldsymbol{r}_j) r^{-+}_{j,M'M}(k',k) & z < z_j - d/2 \\ \sum_{M'} \int dk' \chi^+_{M'k'}(\boldsymbol{r}_j) t^{++}_{j,M'M}(k',k) & z > z_j + d/2 \end{cases}$$
$$\Psi^-_{Mk}(\boldsymbol{r}) = \begin{cases} \chi^-_{Mk}(\boldsymbol{r}_j) + \sum_{M'} \int dk' \chi^+_{M'k'}(\boldsymbol{r}_j) r^{+-}_{j,M'M}(k',k) & z > z_j + d/2 \\ \sum_{M'} \int dk' \chi^-_{M'k'}(\boldsymbol{r}_j) t^{--}_{j,M'M}(k',k) & z < z_j - d/2 \end{cases} \tag{A.1}$$

where $\boldsymbol{r}_j = \boldsymbol{r} - z_j\hat{\boldsymbol{z}}$. The reflectivity is found by recursively applying for $j = n-1, \ldots, 1$

$$r^{-+}_{j,n} = r^{-+}_j + t^{--}_j p^-_{j+1} r^{-+}_{j+1,n} p^+_j \left(1 - r^{+-}_j p^-_{j+1} r^{-+}_{j+1,n} p^+_j\right)^{-1} t^{++}_j, \tag{A.2}$$

which gives the reflectivity of the combined region comprising slabs j through n, $r^{-+}_{j,n}$, in terms of the scattering proper-

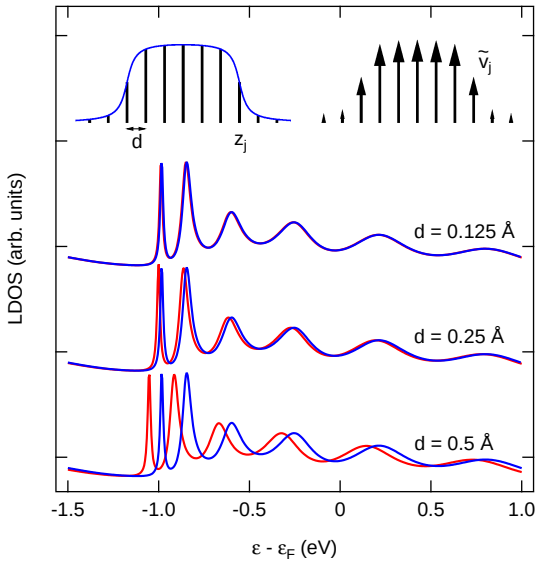

FIG. 6. (Color online) Calculated LDOS above a void (cylindrical volume, height 8 Å, radius 25 Å, potential $v = 13.6$ eV, depth 11.4 Å) obtained using different δ-disk spacings d (red, vertically offset for clarity). In each case shown in blue is the LDOS obtained with $d = 0.015625$ Å. Left inset: Partitioning of void into slices, which in isolation scatter cylindrical waves. The void potential is depicted as a solid line. Right inset: Replacement of void potential by δ disks with strength $\tilde{v}_j$.

ties of slice j and the reflectivity $r^{-+}_{j+1,n}$. The void reflectivity is $\mathcal{R} = r^{-+}_{1,n}$. Use of Eq. (A.2) starts with $r^{-+}_{n,n} = r^{+-}_{n}$, multiplication corresponds to, *e. g.*,

$$a\,b \to \sum_{M'} \int dk' a_{MM'}(k,k') b_{M'M''}(k',k''), \qquad \text{(A.3)}$$

and the propagator $p^{\pm}_j = e^{\pm i\kappa(z_{j\pm1}-z_j)}\delta_{MM'}\delta(k-k')$. The scattering matrices of each individual segment are found from the Lippmann-Schwinger equation $\Psi^{\pm} = \chi^{\pm} + G_0 v \Psi^{\pm}$ where

$$G_0(\boldsymbol{r},\boldsymbol{r}';\varepsilon) = \sum_M \int dk \chi_{Mk}(\boldsymbol{R})\chi^*_{Mk}(\boldsymbol{R}')(-i/\kappa)e^{i\kappa|z-z'|}. \qquad \text{(A.4)}$$

It is convenient to replace the potential v in each segment by a "δ-disk" such that $v(\boldsymbol{r}) \to \tilde{v}_j(\boldsymbol{R})\delta(z-z_j)$, $|z-z_j| < d/2$ where

$$\tilde{v}_j(\boldsymbol{R}) = \int_{z_j-d/2}^{z_j+d/2} v(\boldsymbol{r}) dz. \qquad \text{(A.5)}$$

Then formally $r^{-+}_j = r^{+-}_j = (i\kappa - \tilde{v}_j)^{-1}\tilde{v}_j$ and $t^{++}_j = t^{--}_j = 1 + r^{-+}_j$, where

$$\tilde{v}_{j,MM'}(k,k') = \int d^2\boldsymbol{R}\chi^*_{Mk}(\boldsymbol{R})\tilde{v}_j(\boldsymbol{R})\chi_{M'k'}(\boldsymbol{R}) \qquad \text{(A.6)}$$

and $i\kappa = i\kappa\delta_{MM'}\delta(k-k')$. This obviates the need to solve a couple-channel equation. As $d \to 0$, $\tilde{v}_j \to 0$ and it is straightforward to show that the scattering matrices given by the δ-disks converge to those of the Born approximation, and correspondingly that in this limit the reflectivity $r^{-+}_{1,n}$ converges to the exact reflectivity of the void potential. Figure 6 illustrates the convergence with δ-disk thickness. Typically we use $d = 0.0625$ Å. κ becomes imaginary for $k > \sqrt{2\varepsilon}$ causing the propagators $p^{\pm}_j$ to decay exponentially, providing a natural cut-off for k integrations. Numerically, for energies close to ε_F we use 512 or 1024 regularly spaced k-values extending out to $1.8\sqrt{2\varepsilon}$.

* s.crampin@bath.ac.uk
† joerg.kroeger@tu-ilmenau.de

[1] S. A. Wolf, D. D. Awschalom, R. A. Buhrman, J. M. Daughton, S. von Molnár, M. L. Roukes, A. Y. Chtchelkanova, and D. M. Treger, Science **294**, 1488 (2001).
[2] G. Burkard, H.-A. Engel, and D. Loss, "Spintronics, quantum computing, and quantum communication in quantum dots," in *Fundamentals of Quantum Information: Quantum Computation, Communication, Decoherence and All That*, edited by D. Heiss (Springer, Berlin, Heidelberg, 2002) pp. 241–265.
[3] G. Konstantatos, *Colloidal quantum dot optoelectronics and photovoltaics* (Cambridge University Press, Cambridge, 2013).
[4] S. Nakamura, Rev. Mod. Phys. **87**, 1139 (2015).
[5] P. V. Kamat, J. Phys. Chem. Lett. **4**, 908 (2013).
[6] J. Zhao, M. A. Holmes, and F. E. Osterloh, ACS Nano **7**, 4316 (2013).
[7] R. E. Thomas, J. Appl. Phys. **41**, 5330 (1970).
[8] M. Milun, P. Pervan, and D. P. Woodruff, Rep. Prog. Phys. **65**, 99 (2002).
[9] J. J. Paggel, T. Miller, and T.-C. Chiang, Science **283**, 1709 (1999).
[10] X. Ma, P. Jiang, Y. Qi, J. Jia, Y. Yang, W. Duan, W.-X. Li, X. Bao, S. B. Zhang, and Q.-K. Xue, Proc. Natl. Acad. Sci. U.S.A. **104**, 9204 (2007).
[11] L. Aballe, A. Barinov, A. Locatelli, S. Heun, and M. Kiskinova, Phys. Rev. Lett. **93**, 196103 (2004).
[12] Y. Jia, M. Özer, H. Weitering, and Z. Zhang, "Nanophenomena at surfaces: Fundamentals of exotic condensed matter properties," (Springer, Berlin, 2011) Chap. Quantum Size Effects in the Growth and Properties of Ultrathin Metal Films, Alloys, and Related Low-Dimensional Structures, pp. 67–112.
[13] J. E. Ortega, F. J. Himpsel, G. J. Mankey, and R. F. Willis, Phys. Rev. B **47**, 1540 (1993).
[14] C. Carbone, E. Vescovo, O. Rader, W. Gudat, and W. Eberhardt, Phys. Rev. Lett. **71**, 2805 (1993).
[15] A. F. Santander-Syro, F. Fortuna, C. Bareille, T. C. Rodel, G. Landolt, N. C. Plumb, J. H. Dil, and M. Radovic, Nat. Mater. **13**, 1085 (2014).
[16] D. Eom, S. Qin, M.-Y. Chou, and C. K. Shih, Phys. Rev. Lett. **96**, 027005 (2006).

[17] Y. Guo, Y.-F. Zhang, X.-Y. Bao, T.-Z. Han, Z. Tang, L.-X. Zhang, W.-G. Zhu, E. G. Wang, Q. Niu, Z. Q. Qiu, J.-F. Jia, Z.-X. Zhao, and Q.-K. Xue, Science **306**, 1915 (2004).

[18] S. Qin, J. Kim, Q. Niu, and C.-K. Shih, Science **324**, 1314 (2009).

[19] A. Zhao, Q. Li, L. Chen, H. Xiang, W. Wang, S. Pan, B. Wang, X. Xiao, J. Yang, J. G. Hou, and Q. Zhu, Science **309**, 1542 (2005).

[20] T. Uchihashi, J. Zhang, J. Kröger, and R. Berndt, Phys. Rev. B **78**, 033402 (2008).

[21] M. F. Crommie, C. P. Lutz, and D. M. Eigler, Nature **363**, 524 (1993).

[22] Y. Hasegawa and Ph. Avouris, Phys. Rev. Lett. **71**, 1071 (1993).

[23] P. Avouris and I.-W. Lyo, Science **264**, 942 (1994).

[24] M. F. Crommie, C. P. Lutz, and D. M. Eigler, Science **262**, 218 (1993).

[25] E. J. Heller, M. F. Crommie, C. P. Lutz, and D. M. Eigler, Nature **369**, 464 (1994).

[26] J. Kliewer, R. Berndt, and S. Crampin, New J. Phys. **3**, 22 (2001).

[27] J. Li, W. D. Schneider, R. Berndt, and S. Crampin, Phys. Rev. Lett. **80**, 3332 (1998).

[28] C. Tournier-Colletta, B. Kierren, Y. Fagot-Revurat, and D. Malterre, Phys. Rev. Lett. **104**, 016802 (2010).

[29] H. Jensen, J. Kröger, R. Berndt, and S. Crampin, Phys. Rev. B **71**, 155417 (2005).

[30] S. Crampin, H. Jensen, J. Kröger, L. Limot, and R. Berndt, Phys. Rev. B **72**, 035443 (2005).

[31] B. N. Taber, C. F. Gervasi, J. M. Mills, D. A. Kislitsyn, E. R. Darzi, W. G. Crowley, R. Jasti, and G. V. Nazin, J. Phys. Chem. Lett. **7**, 3073 (2016).

[32] K. Müller, M. Enache, and M. Stöhr, J. Phys.: Condens. Matter **28**, 153003 (2016).

[33] L. Bürgi, O. Jeandupeux, A. Hirstein, H. Brune, and K. Kern, Phys. Rev. Lett. **81**, 5370 (1998).

[34] A. Mugarza, A. Mascaraque, V. Pérez-Dieste, V. Repain, S. Rousset, F. J. García de Abajo, and J. E. Ortega, Phys. Rev. Lett. **87**, 107601 (2001).

[35] A. Mugarza and J. E. Ortega, J. Phys.: Condens. Matter **15**, S3281 (2003).

[36] N. Zaki, K. Knox, P. D. Johnson, J. Fujii, I. Vobornik, G. Panaccione, and R. M. Osgood, Phys. Rev. B **83**, 205420 (2011).

[37] S. K. Hämäläinen, Z. Sun, M. P. Boneschanscher, A. Uppstu, M. Ijäs, A. Harju, D. Vanmaekelbergh, and P. Liljeroth, Phys. Rev. Lett. **107**, 236803 (2011).

[38] S.-h. Phark, J. Borme, A. L. Vanegas, M. Corbetta, D. Sander, and J. Kirschner, ACS Nano **5**, 8162 (2011).

[39] S. J. Altenburg, J. Kröger, T. O. Wehling, B. Sachs, A. I. Lichtenstein, and R. Berndt, Phys. Rev. Lett. **108**, 206805 (2012).

[40] D. Subramaniam, F. Libisch, Y. Li, C. Pauly, V. Geringer, R. Reiter, T. Mashoff, M. Liebmann, J. Burgdörfer, C. Busse, T. Michely, R. Mazzarello, M. Pratzer, and M. Morgenstern, Phys. Rev. Lett. **108**, 046801 (2012).

[41] W. Jolie, F. Craes, M. Petrović, N. Atodiresei, V. Caciuc, S. Blügel, M. Kralj, T. Michely, and C. Busse, Phys. Rev. B **89**, 155435 (2014).

[42] W. Jolie, F. Craes, and C. Busse, Phys. Rev. B **91**, 115419 (2015).

[43] N. Nilius, T. M. Wallis, and W. Ho, Science **297**, 1853 (2002).

[44] S. Fölsch, P. Hyldgaard, R. Koch, and K. H. Ploog, Phys. Rev. Lett. **92**, 056803 (2004).

[45] S. Fölsch, J. Yang, C. Nacci, and K. Kanisawa, Phys. Rev. Lett. **103**, 096104 (2009).

[46] J. Yang, C. Nacci, K. Kanisawa, and S. Fölsch, J. Vac. Sci. Technol. B **28**, C5G1 (2010).

[47] N. Néel, R. Berndt, J. Kröger, T. O. Wehling, A. I. Lichtenstein, and M. I. Katsnelson, Phys. Rev. Lett. **107**, 106804 (2011).

[48] E. H. Do and H. W. Yeom, Phys. Rev. Lett. **115**, 266803 (2015).

[49] J. Repp, P. Liljeroth, and G. Meyer, Nat. Phys. **6**, 975 (2010).

[50] S. Wang, W. Wang, and N. Lin, Phys. Rev. Lett. **106**, 206803 (2011).

[51] S. R. Schofield, P. Studer, C. F. Hirjibehedin, N. J. Curson, G. Aeppli, and D. R. Bowler, Nat. Commun. **4**, 1649 (2013).

[52] I. Swart, P. Liljeroth, and D. Vanmaekelbergh, Chem. Rev. **116**, 11181 (2016).

[53] V. Lindberg and B. Hellsing, J. Phys.: Condens. Matter **17**, S1075 (2005).

[54] W. Zhou and J. J. Coleman, Curr. Opin. Solid State Mater. Sci. **20**, 352 (2016).

[55] J. Mannhart, H. Boschker, T. Kopp, and R. Valentí, Rep. Prog. Phys. **79**, 084508 (2016).

[56] G. Reecht, H. Bulou, F. Scheurer, V. Speisser, B. Carrière, F. Mathevet, and G. Schull, Phys. Rev. Lett. **110**, 056802 (2013).

[57] Y. Zhao, J. Wyrick, F. D. Natterer, J. F. Rodriguez-Nieva, C. Lewandowski, K. Watanabe, T. Taniguchi, L. S. Levitov, N. B. Zhitenev, and J. A. Stroscio, Science **348**, 672 (2015).

[58] M. Müller, N. Néel, S. Crampin, and J. Kröger, Phys. Rev. Lett. **117**, 136803 (2016).

[59] M. Schmid, W. Hebenstreit, P. Varga, and S. Crampin, Phys. Rev. Lett. **76**, 2298 (1996).

[60] O. Kurnosikov, O. A. O. Adam, H. J. M. Swagten, W. J. M. de Jonge, and B. Koopmans, Phys. Rev. B **77**, 125429 (2008).

[61] O. Kurnosikov, D. V. Kulikov, V. S. Kharlamov, H. J. M. Swagten, and Yu. V. Trushin, Phys. Rev. B **84**, 054109 (2011).

[62] O. Kurnosikov, J. H. Nietsch, M. Sicot, H. J. M. Swagten, and B. Koopmans, Phys. Rev. Lett. **102**, 066101 (2009).

[63] O. Kurnosikov, H. J. M. Swagten, and B. Koopmans, Phys. Rev. Lett. **106**, 196803 (2011).

[64] C. Sprodowski and K. Morgenstern, Phys. Rev. B **82**, 165444 (2010).

[65] S. J. Clark, M. D. Segall, C. J. Pickard, P. J. Hasnip, M. I. J. Probert, K. Refson, and M. C. Payne, Z. Kristall. **220**, 567 (2005).

[66] M. Hupalo and M. C. Tringides, Phys. Rev. B **65**, 115406 (2002).

[67] R. Otero, A. L. Vázquez de Parga, and R. Miranda, Phys. Rev. B **66**, 115401 (2002).

[68] M. Becker and R. Berndt, Appl. Phys. Lett. **96**, 033112 (2010).

[69] J. H. Dil, T. U. Kampen, B. Hülsen, T. Seyller, and K. Horn, Phys. Rev. B **75**, 161401(R) (2007).

[70] F. Yndurain and M. P. Jigato, Phys. Rev. Lett. **100**, 205501 (2008).

[71] M. Becker and R. Berndt, Phys. Rev. B **81**, 205438 (2010).

[72] J. Kröger, L. Limot, H. Jensen, R. Berndt, S. Crampin, and E. Pehlke, Progress in Surface Science **80**, 26 (2005).

[73] J. Kröger, M. Becker, H. Jensen, T. von Hofe, N. Néel, L. Limot, R. Berndt, S. Crampin, E. Pehlke, C. Corriol, V. Silkin, D. Sánchez-Portal, A. Arnau, E. Chulkov, and P. Echenique, Progress in Surface Science **82**, 293 (2007).